Check for updates

Geochemistry, Geophysics, Geosystems®

AGU ADVANCING EARTH AND SPACE SCIENCE

RESEARCH ARTICLE
10.1029/2021GC009711

Kinetics and Mechanisms of Acid-pH Weathering of Pyroxenes

L. Monasterio-Guillot[1], C. Rodriguez-Navarro[1], and E. Ruiz-Agudo[1]

[1]Department of Mineralogy and Petrology, University of Granada, Granada, Spain

Key Points:

- Acidic weathering of pyroxenes occurs by crack formation and propagation by stress corrosion
- Fracture formation and propagation is essential to this weathering process, as it facilitates fluid transport within impermeable materials
- The formation of M-S-H phases reduce the yield of carbonation, which acts as a handicap for an effective Geological Carbon Storage strategy

Supporting Information:

Supporting Information may be found in the online version of this article.

Correspondence to:

E. Ruiz-Agudo,
encaruiz@ugr.es

Citation:

Monasterio-Guillot, L., Rodriguez-Navarro, C., & Ruiz-Agudo, E. (2021). Kinetics and mechanisms of acid-pH weathering of pyroxenes. *Geochemistry, Geophysics, Geosystems*, *22*, e2021GC009711. https://doi.org/10.1029/2021GC009711

Received 23 FEB 2021
Accepted 14 SEP 2021

© 2021. The Authors.
This is an open access article under the terms of the Creative Commons Attribution-NonCommercial-NoDerivs License, which permits use and distribution in any medium, provided the original work is properly cited, the use is non-commercial and no modifications or adaptations are made.

Abstract Weathering of primary silicate minerals under acidic conditions occurs in contexts as varied as acid mine drainage, volcanic environments, soils, stone monuments subjected to acid rain or Geological Carbon Storage (GCS). Considering the abundance of pyroxenes on the Earth crust, knowledge of their weathering kinetics and mechanisms may help to optimize carbonate yield in GCS. Here we report experimental results from the reaction of the clinopyroxenes augite and diopside in acidic solutions. Dissolution at far-from-equilibrium conditions results in the formation of etch pits where crack initiate and propagate by stress corrosion and pressure exerted by swelling of an amorphous, gel-like Si-rich phase, which precipitates despite the undersaturation of the bulk solution and whose formation is highly controlled by the heterogeneity of the mineral surface and the local transport mechanism. These precipitates are commonly localized within deep etch pits and cracks, characterized by a low fluid renewal where high Si-concentrations can be reached locally, so that supersaturation with respect to amorphous silica can occur. Cracks and silica precipitates are most abundant in the case of augite weathered in flow-through experiments. This is related to its faster reaction rate compared to diopside, most likely due to its higher iron content. Finally, in the case of diopside an amorphous magnesium silicate hydrate (M-S-H) precursor forms, which represents an indirect evidence of the high pH conditions prevailing at the diopside-solution interface during dissolution.

1. Introduction

Pyroxenes are among the main constituent of basic and ultrabasic igneous rocks. Because they form at high *P* and *T* conditions They are not thermodynamically in equilibrium at the Earth surface and will transform into more stable phases by an irreversible thermodynamic process (Frings & Buss, 2019). Weathering is a first-order process that enables life on Earth, as the solutes released during chemical weathering serve as nutrients, and these reactions represent the first step of the biogeochemical cycle of most elements (Frings & Buss, 2019). In this sense, chain silicates are important contributors of Mg, Ca and Fe to natural waters (Marini, 2006). Also, the kinetics of primary silicate chemical weathering controls erosion rates and soil formation (Frings & Buss, 2019). Weathering of Ca, Mg-containing silicates is as well of relevance due to its role in controlling the composition of the atmosphere acting as long-term sink for CO_2, and therefore in the global climate (e.g., Chen & Brantley, 1998).

Chemical weathering under acidic conditions occurs in a wide range of scenarios on Earth, including volcanic environments, soils as well as monument stones subjected to acid rain (Simão et al., 2006), or acid mine drainage sites (e.g. Hellmann et al., 2012). Additionally, from a technological point of view, these pH conditions are relevant for *in situ* geological CO_2 storage in rocks (pH around 3, Shao et al., 2013). This process requires the release of the divalent metal cations contained in the structure of the silicate mineral, which then react with dissolved CO_2 and precipitate as carbonates (mineral carbonation, Daval et al., 2009). The rate limiting step for this process is considered to be the release of divalent cations from the silicate structure, and in the specific case of pyroxenes, their low reactivity is claimed to be responsible for the overall low conversion into carbonates, compared for example with olivine and serpentine under similar conditions (Meyer, 2014). Thus, knowledge of the kinetics and mechanisms of pyroxene weathering under different experimental conditions may help to optimize the conditions to obtain maximum carbonate yields.

Despite the importance of the weathering of Ca, Mg-bearing pyroxenes, there are relatively few studies that have addressed the dissolution kinetics of these minerals, and in particular of augite (Schott & Berner, 1985; Siegel & Pfannkuch, 1984), as compared to other minerals such as feldspars or olivine. Also, there

are significant differences between experimentally determined rates reported by different researchers. Such differences may arise from several causes, including differences in mineral composition, saturation state, pre-treatment of the minerals, and, notably, their (assumed, see below) non-stoichiometric dissolution and the formation of Si-rich surface altered layers (SALs), among others (Brantley & Chen, 1995). SALs are nano-to micrometer thick layers at the surface of the minerals with a different composition and texture, which are commonly amorphous and silica-rich. They play a key role in controlling weathering rates of silicates since they may result in the passivation of the surface and the arrest of the process and therefore, the non-effective and continuous release of cations to the solution to complete the carbonation of the silicate minerals (Banfield et al., 1995; Casey et al., 1989; Daval et al., 2011; Hellmann et al., 2012; Knauss et al., 1993; Monasterio-Guillot et al., 2019; Ruiz-Agudo et al., 2014, 2016; Schott et al., 2012).

Although early studies suggest that SALs form by a mechanism in which alkali-earth metals are preferentially released to the solution and exchanged for H^+ by a diffusion-reaction forming of a cation-depleted surface layer, called "leached layer" (Banfield et al., 1995; Casey et al., 1989; Schott et al., 2012; Weissbart & Rimstidt, 2000), an increasing number of studies are reporting experimental evidence that is in better agreement with a mechanism whereby SALs form by a tightly coupled interfacial dissolution–precipitation process (ICDP, Daval et al., 2009, 2010; Hellmann et al., 2012). This latter mechanism relies on the establishment of strong compositional gradients at the mineral-solution interface, which has been hypothesized to depend on the relative rates of mass transport and surface reaction in the system. Here, we further evaluate this hypothesis using two abundant clinopyroxenes: diopside ($CaMgSi_2O_6$) and augite $(Ca,Na)(Mg,Fe,Al)(Si,Al)_2O_6$). Comparatively to other silicates such as wollastonite ($CaSiO_3$), the minerals investigated here present lower reactivity, are more representativity of the Earth's crust, and have been poorly studied (Daval et al., 2010; Dixit & Carroll, 2007; Knauss et al., 1993; Richet et al., 1998; Schott & Berner, 1985; Stockmann et al., 2008). This study seeks to gain some insight on (a) the actual mechanisms of pyroxene dissolution and SALs formation at low pH and the effect of (b) the hydrodynamic conditions and (c) the compositional differences of the starting material on the kinetics and mechanism of pyroxene dissolution.

2. Materials and Methods

2.1. Starting Materials

Single crystals of diopside ($Ca_{0.97}Mg_{0.84}Fe_{0.17}Si_2O_6$) and augite ($Na_{0.05}Ca_{0.86}Mg_{0.76}Fe_{0.23}Ti_{0.07}Al_{0.3}Si_{1.7}O_6$) from museum collection and uncertain origin of optical quality were cut in fragments of $1 \times 1 \times 1$ mm in size with a diamond saw. Indexed electron backscattering diffraction (EBSD) pattern were analyzed on unreacted crystals by field emission scanning electron microscopy (FESEM, Auriga Carl Zeiss SMT). During EBSD analysis the electron beam was normal to the {001} and {010} faces of augite and diopside, respectively. Their composition was determined by ion-coupled plasma optical emission spectrometry (ICP-OES, Perkin Elmer, Optima 8300) analysis of the solution obtained upon full digestion of the unreacted mineral using HF and HCl (5M). No other minor phases were detected by X-ray diffraction (XRD) in diopside crystals (Figure S1 in Supporting Information S1). However, minor inclusions of ilmenite ($FeTiO_3$) were observed in augite crystals. Crystals were analyzed using an X'Pert PRO diffractometer (PANalytical) with the following instrumental parameters: Cu Kα-radiation ($\lambda = 1.5405$ Å), current = 40 mA, acceleration voltage = 45 kV, measurement range = 3–70 °2θ, time per step = 4 s, and step size = 0.04 °2θ. Diffraction patterns were analyzed using the computer code HighScore Plus 2.2.4 (PANalytical) and identified matching the experimental diffraction peaks with those included in the Joint Committee for Powder Diffraction Standards (JCPDS) PDF-2 database. The reacting solutions were prepared immediately before the experiments using Milli-Q water (resistivity 18.2 MΩ·cm, Millipore) adjusted to pH 1.5 using HCl (Sigma, Puriss). The absence of calcium, magnesium, and silicon in the input solutions ensures far-from-equilibrium conditions concerning the original materials.

2.2. Flow-Through and Batch Dissolution Experiments

Flow-through dissolution experiments were performed using PTFE vessels (polytetrafluoroethylene, $V_{tot} = 30$ mL) where one fragment of each crystal per reactor (0.0051–0.0058 g weight) was placed. The reacting solutions where heated at 80 °C and passed over the crystals at a flow rate of 2 mL/min during

10 hr. This temperature was selected in order to have a significant reaction during the course of the experiments. The short reaction times are intended to be able to study the early stages of pyroxene dissolution. Ten mL aliquots of effluent solution were continuously collected in 5 min batches. For batch experiments, a single crystal was introduced in each PTFE vessels (polytetrafluoroethylene, $V_{tot} = 3$ mL) and 1 mL of the reacting solution was added to the reactor before the beginning of the experiments. The PTFE vessels were subsequently introduced into steel reactors, sealed and heated to 80°C for 10 h. Reactors were then cooled at room T and opened. Crystals were separated and introduced in absolute ethanol (99.8%, Sigma Aldrich) to immediately dry the hydrated silica and avoid the typical structural changes associated with standard oven drying. To ensure reproducibility, each experiment was performed in duplicate.

2.3. Analysis of the Solutions After Weathering Experiments

The pH of the solutions was measured immediately after the dissolution experiments using a glass electrode (Metrohm) calibrated with three standard solutions (pH = 4.01, 7.01 and 10.01 at 25°C) with ±0.01 of uncertainty. The concentrations of Ca, Mg and Si in the solutions after the reactions were determined by ICP-OES at Centro de Instrumentación Científica (CIC-UGR). Dissolution rates of calcium, magnesium, and silicon in flow-through experiments were calculated using the mass balance adapted from Daval et al. (2010) written as follows:

$$r_i = \frac{\nu \left[i \right]}{\eta_i \, SSA \, m_o} \tag{1}$$

where ν is the flow rate of the solution ($m^3\ s^{-1}$), $\left[i \right]$ is the concentration of the selected ion in the effluent solution ($mol\ m^{-3}$), η_i is the stoichiometric coefficient of element i in the mineral, SSA is the surface area exposed to the solution ($m^2\ g^{-1}$) and m_o is the initial mass of the mineral (g). The value of surface area used in this study was obtained by multiplying the geometric area of the crystals by the roughness factor given by Stockmann et al. (2008). Dissolution rates in batch experiments were determined using the following equation:

$$r_i = \frac{V \left[i \right]}{\eta_i \, SSA \, t \, m_o} \tag{2}$$

where V is the volume of the solution in the reactor (m^3), $\left[i \right]$ is the concentration of the selected ion in the solution at the end of the experiments ($mol\ m^{-3}$), η_i is the stoichiometric coefficient of element i in the mineral, SSA is the surface area exposed to the solution ($m^2\ g^{-1}$), t is the duration of the experiments (36,000 s) and m_o is the initial mass of the mineral (g).

Calculation of solution speciation and saturation indexes with respect to relevant phases (augite, diopside, amorphous silica and magnesium silicate hydrate, M-S-H) was performed using PHREEQC computer code (version 3.3.12, USGS, Reston, VA, USA) and the lnll.dat database (Parkhurst & Appelo, 1999). The solubility product constants and dissolution reactions for augite, diopside, amorphous silica and M-S-H used in this study are shown in Table S1 in Supporting Information S1.

2.4. Characterization of Reacted Solids

Solids were analyzed by Fourier transform infrared spectroscopy using an attenuated total reflectance sample holder (ATR-FTIR, Jasco) in the spectral range 400–4,000 cm^{-1} with a step size of 0.48 cm^{-1}. Reported spectra correspond to the average of 132 accumulations. Penetration depths in ATR-FTIR typically ranges from 0.6 to 2 μm. The distribution of silica monomers, oligomers, and polymers was calculated using FITYK software for data processing and non-linear curve fitting (Wojdyr, 2010). Gaussian fit was performed using Equation 3:

$$y = a_0 \exp - \ln(2)\left[\left(\frac{x - a_1}{a_2}\right)^2\right] \quad (3)$$

where a_0 is the height of the peak, a_1 is the full width at half maximum (FWHM) and a_2 is the standard deviation: $a_2 = \sqrt{2 \ln 2}\,\sigma$. Subsequently, areas of the different bands were integrated and normalized to the total area to calculate the distribution (in %) of the different silica species on the surface of the crystals. A minimum of two surfaces per mineral and experimental condition (batch/flow-through) were analyzed by FTIR.

In addition, solids were analyzed by scanning electron microscopy (SEM) using a FEI Quanta 400 SEM for morphology and texture determination, coupled to an X-ray energy dispersive spectrometer (EDS, xFlash Bruker) working at an acceleration voltage of 20 kV for microanalysis. Surfaces were imaged in secondary electron mode with working distances between 9 and 11 mm. Reacted samples were further characterized by X-ray micro-computed tomography (micro-CT) using a Xradia 510 (VERSA ZEISS) for the analysis of the spatial distribution and quantification of secondary phases using high-resolution contrast images. Scans were performed at 40 kV and 5 μA. Data were acquired with a 4x magnification CCD objective for a total scan time of 15 h including the collection of reference images. The voxel size achieved under these conditions was 3 μm. It should be noted that micro-CT analyses were performed on the same crystals first analyzed by SEM-EDX to avoid any potential error on the selection of the gray-level/contrast threshold to quantify the selected phases. The image analysis was performed using Dragonfly (Version 4.1, Object Research Systems) software. Finally, solid products were studied by means of transmission electron microscopy (TEM) using a FEI Titan operating at 300 kV and equipped with a high angle annular dark field detector (HAADF). Selected area electron diffraction (SAED) patterns and EDS analyses (STEM mode) were performed to determine the crystalline structure and the chemical composition of the reacted samples, respectively. Samples were prepared using crushed solids suspended in 5 mL of absolute ethanol (99.8%, Sigma Aldrich) and dispersed in an ultrasound bath for 120 s, and fished from the beaker using Formvar ® film-coated Cu grids. Additionally, elemental mole ratios of the alteration products were determined by analytical electron microscopy (AEM) using the thin foil method and experimental k factors (Cliff & Lorimer, 1975). k factors were obtained experimentally from silicate standards. For Al, the k factor (1.00 +- 0.02), was determined experimentally using: albite, anorthite, anorthoclase, augite, biotite, scapolite, spessartine, microcline, muscovite, osumilite and introduced in the software. For Mg, the k factor (1.10 +- 0.03) was determined experimentally using augite, biotite, olivine and osumilite standards. For, Ca the k factor (1.21 +- 0.04) was determined experimentally using anorthite, scapolite and titanite. For Fe, the k factor (1.37 +- 0.03) was determined experimentally using augite, biotite, olivine, rhodonite and osumilite.

3. Results

3.1. ATR-FTIR Analysis and Silicate Species Distribution in Unreacted and Reacted Pyroxenes

IR spectra of silicates show a series of characteristics bands, called Reststrahlen bands (RBs), which are the results of strong fundamental molecular vibrations. For silicates, RBs appear at ~700–1,100 cm^{-1} (asymmetric stretching vibrations of SiO_4 units) and approx. at 400–700 cm^{-1} (bending vibrations). Its exact position is sensitive to the silicate structure (Fu et al., 2017). In our experiments, ATR-FTIR spectra of unreacted augite and diopside (Figures 1a and 1b) showed two bands at ~615 and 630 and 670 cm^{-1}, corresponding to O(nonbridging)-Si-O(nonbridging) bending and a mixed stretching-bending mode of Si-O-Si bridging bond (Richet et al., 1998 and references therein). A broad band spanning from ~685 to 985 cm^{-1} in augite and 680-970 cm^{-1} in diopside that corresponds to the ν_3 asymmetric stretching of Si-O was also observed. Finally, two bands located at 1,029–1,056 cm^{-1}, and 946–950 cm^{-1} corresponding to the Si-O-Si stretching vibration and the ν_3 vibration of Si-O bond in crystalline silicates, respectively, were also found.

IR spectra of augite samples after batch and flow-dissolution experiments (Figure 1a) are very similar. The bands located at 628 and 666 cm^{-1} appeared less defined and with lower intensity. The ν_3 Si-O asymmetric stretching band appears smoother and suffered a broadening and a reduction in intensity as compared with the ν_3 band of the unreacted material, changing slightly its position from ~685 to 929 cm^{-1} to ~685 to 939 cm^{-1}. In the case of diopside, after both batch and flow-through dissolution experiments (Figure 1b),

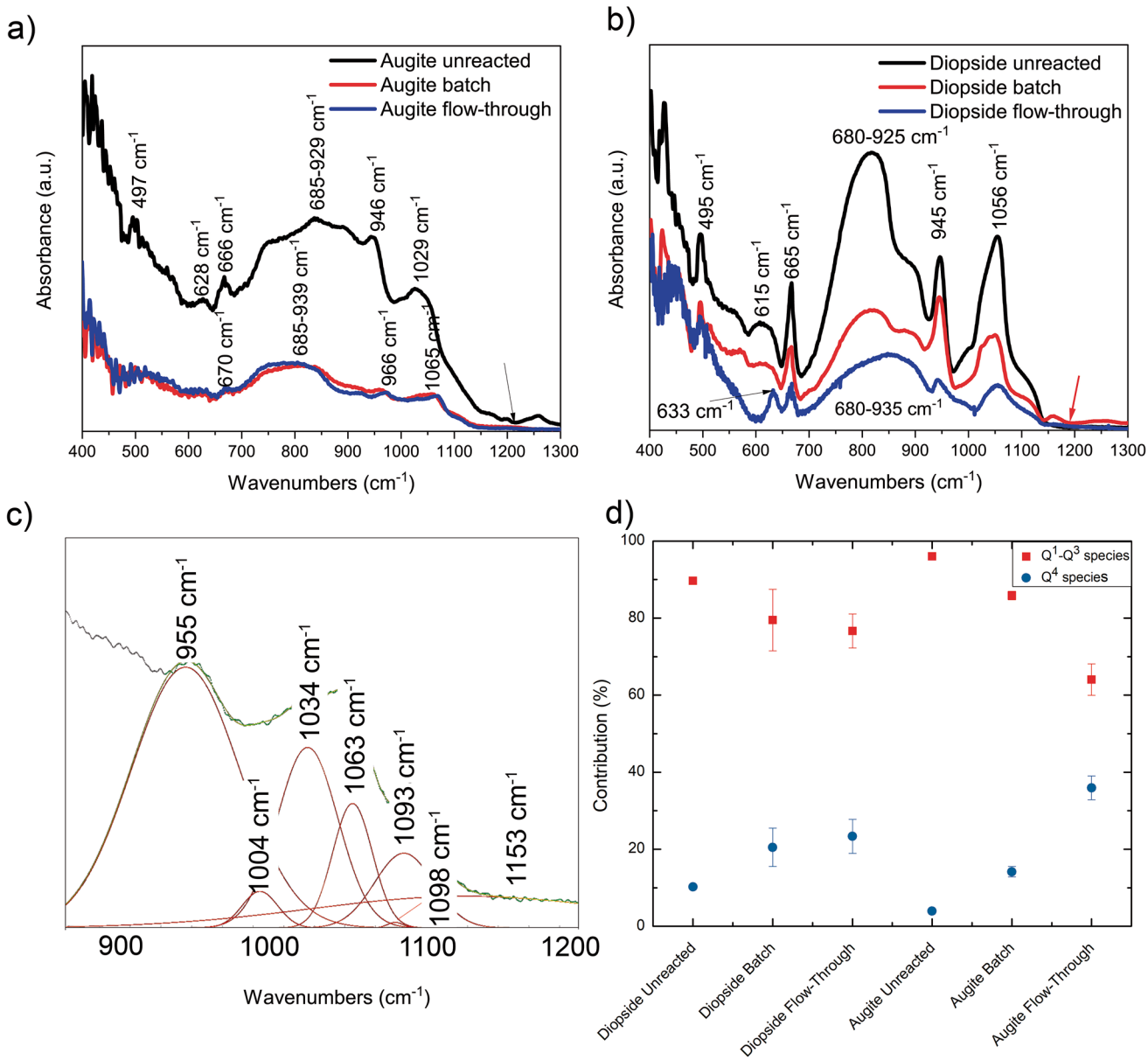

Figure 1. FTIR analyses of unreacted and reacted samples. (a) FTIR spectra of unreacted and reacted augite. (b) FTIR spectrum of unreacted and reacted diopside. (c) Example of FITYK Gaussian fitting to the different Q^n species of the FTIR spectrum corresponding to augite subjected to dissolution under flow-through experiments. (d) Q^1–Q^3 and Q^4 species contribution in the reacted and unreacted crystals summing-up the total area of the integrated peaks of ATR-FTIR spectra after FITYK peak fitting. For Q^n notation, see below.

the main changes in the spectra are related to the broadening, smoothing and decrease in intensity of the different bands, particularly the broad band corresponding to the ν_3 asymmetric stretching of Si-O bond (~892–705 cm^{-1} in unreacted diopside). The position of the bands remains basically unaltered, or with very slight shifts.

The degree of polymerization of SiO_4 tetrahedra in different silicates strongly influences their IR spectra. In a non-polymerized silicate such as olivine, the structure consists of isolated SiO_4 tetrahedra and none of the oxygen atoms is linked to another tetrahedra. Pyroxenes with space group C2/c such as diopside or augite have three different oxygen positions in their structure: the apical non-bridging oxygen O1; the side non-bridging oxygen (nbr) O2 and the bridging oxygen (br) O3, affecting the position of the FTIR bands (Omori, 1971). In a tectosilicate such as quartz the structure consists of a three-dimensional network of SiO_4

tetrahedra with a central silicon atom, surrounded by oxygen atoms with the four oxygen atoms acting as bridges to other tetrahedra (Biswas et al., 2018). The structure of amorphous silica locally resembles that of quartz, but the arrangement of tetrahedra is random, so that not all oxygen atoms are bridging. Shifts of RB bands to higher wavenumbers (blue shifts) are the result of an increase in the bond strength of Si–O, due to an increase in polymerization of the silica units in the silicate structure.

Crystalline silicates possess long-range order, with well-defined Si-O bond angles and lengths for all SiO_4 units. Differences in site symmetry of the SiO_4 units are the responsible of the vibrational fine structure. By contrast, amorphous materials have only short-range order. This results in a broader distribution of Si-O bond angles and lengths when all SiO_4 tetrahedra in the structure are considered. These distributions result in broad and smooth infrared spectral features (Fu et al., 2017). The sharp bands observed in the IR spectra of the unreacted silicates tend to disappear in the altered materials, which have broader IR spectral bands than the original silicates. This observation indicates structural differences between weathered and unweathered silicates, related to the presence of amorphous materials in the weathered samples. Thus, the broadening and smoothing of the IR bands in weathered materials suggest loss of long-range order in the weathered product and amorphization, while shifting of RBs to higher wavenumbers observed in augite indicates increase of the bond strength of Si–O associated with higher degrees of polymerization, in agreement with the formation of a network of corner-sharing SiO_4 in amorphous silica (see below).

The Q^n notation ($n = 0, 1, 2, 3$ or 4) represents the number of bridging oxygens per Si tetrahedron in silicates (Karlsson et al., 2005). For example, olivine as a nesosilicate has a Q^0 structure, as opposed to quartz, which as a tectosilicate it is composed by Q^4 units. The vibration bands located between 950 and 1,050 cm^{-1} in ATR-FTIR spectra of silicate minerals correspond to Q^1–Q^3 units, while vibration bands corresponding to Q^4 units (amorphous silica) are located above 1,051 cm^{-1} (Yang et al., 2008). The contribution of Q^1–Q^3 and Q^4 units in FTIR spectra of augite and diopside samples, before and after dissolution experiments, can be estimated by peak area measurements using the software FYTIK (Wojdyr, 2010) (Figures 1c and 1d). Peak contribution data from the analyses are reported in Table S2 of Supporting Information S1. Gaussian profiles were used due to the multiple contribution profiles needed to fit the asymmetry of almost all the bands. Only the region of the spectra >900 cm^{-1} was taken into account to avoid possible artifacts related to the contribution of Q^0 monomeric species. Here, it can be observed that Q^1–Q^3 units are dominant in all samples. This is consistent with the pyroxene structure, based on chains of tetrahedra (type T-O) linked by two corners (Q^1 and Q^2 units) and one Ca-Mg octahedral strip unit (Hamilton, 2000). On the other hand, amorphous SiO_2 is composed of tetrahedrons connected via four corner-sharing bridging oxygens constituting Q^4 species forming a homogeneous random network. It can also include Q^3 species due to unsatisfied bridging between surface tetrahedra (Dove et al., 2008). Unreacted diopside and augite showed a higher contribution of Q^1–Q^3 units compared to the weathered material (Figure 1d). An increase in the contribution of Q^4 species present in the surface of the mineral was observed after batch and flow-through dissolution experiments. Interestingly, the contribution of Q^4 was higher in flow-through experiments than in batch experiments, particularly in the case of augite, suggesting a higher degree of silica polymerization related to the higher amount of amorphous silica in the materials weathered in flow through experiments (Karlsson et al., 2005). Although this ATR-FTIR analysis was performed on the surface of the crystals and thus it can only be considered as a semi-quantitative and not absolute analysis, FTIR data and the Q^n contribution analysis presented here corroborate the results obtained by other techniques, described below.

3.2. SEM, TEM and Micro-CT Study of Acid-Weathered Pyroxenes

The results of SEM-EDS analysis of reacted samples are shown in Figure 2 and Figures S2–S5 in Supporting InformationS1). In the case of augite reacted in batch experiments, these analysis confirmed the presence of abundant Si-rich patches on augite reacted in batch experiments, without any detected incorporation of other cations (i.e. Ca, Mg, Fe, Al). These patches showed the typical “mud crack”-like structure of dehydrated amorphous silica gel (Ruiz-Agudo et al., 2014). Dendritic iron-rich precipitates, most likely iron oxy-hydroxides, were observed. This type of precipitates is commonly associated with silica precipitation following augite dissolution in an oxidizing environment (Hoch et al., 1996; Siever & Woodford, 1979). In the case of diopside reacted under the same conditions, abundant etch pits were observed on the surface of the mineral (see inset in Figure 2b). This is an evidence that suggests that surface-reaction is the

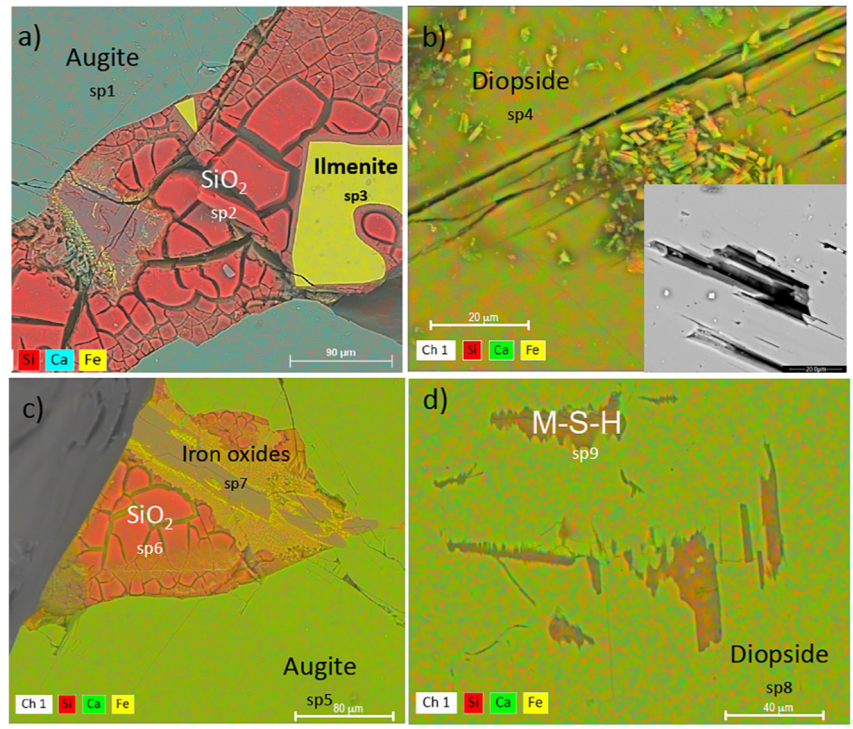

Figure 2. SEM-EDS analyses of reacted samples (a) SEM-EDS elemental map of batch-reacted augite showing amorphous silica (SiO_2) and iron-titanium particles. (b) SEM-EDS spectra of batch-reacted diopside. The inset shows the SEM image of etch pits on the surface of the reacted diopside. (c) SEM-EDS elemental map of augite reacted in flow-through experiments showing amorphous silica (SiO_2) and oxide precipitates. (d) SEM-EDS elemental map of reacted diopside showing amorphous silica. The spectrum of each phase is shown in Figures S2–S5 of Supporting Information S1.

rate-controlling step of the process (Berner et al., 1980). However, no surficial Si-rich layers were evident on reacted diopside. Nevertheless, the mottled, inhomogeneous appearance of the diopside surface seen in the EDS elemental maps could indicate the formation of scarce surface Si-rich precipitates. Very similar textures were observed in augite subjected to flow-through experiments (Figure 2c), and in the case of diopside, the presence of Si-rich phases was limited to the interior of dissolution features (Figure 2d).

TEM-SAED and HAADF-EDS analyses confirmed the presence of a silica-rich phase in contact with weathered augite and diopside crystals in both batch and flow experiments (Figure 3). High-resolution TEM image of partially reacted samples (Figure S10 in Supporting Information S1) show a sharp structural interface between areas with lattice fringes corresponding to the unreacted materials and amorphous secondary precipitates**.** Interestingly, EDS point analyses showed the incorporation of variable amounts of Mg, Fe (and, to a lesser extent, Ca) in the Si-rich phase, in each of the experiments performed as it has been also reported by Daval et al. (2011) **(**Figures S6–S9 in Supporting Information S1). Elemental mole ratios of the alteration products in augite determined by AEM were very close to those of pure amorphous silica (O/Si ≈ 2, see Table S3 and Figure S11 in Supporting Information S1). Despite the similar Mg/Si ratios in both unaltered minerals, the Si-rich phases formed during diopside dissolution showed higher Mg/Si and Fe/Si ratios (Mg/Si = 0.28–0.36 and Fe/Si = 0.10–0.21) than those of the SiO_2 (am) formed during augite dissolution (Mg/Si = 0.03–0.14 and Fe/Si = 0.03–0.10). Mg/Si are lower than those of the unaltered materials (augite: Mg/Si = 0.45; diopside: Mg/Si = 0.42), and Fe/Si ratios are similar (augite: Fe/Si = 0.13; diopside: Fe/Si = 0.09). Note, however, that Fe was not homogenously included within the matrix of this amorphous silica phase, but it was present in the form of nanoparticles (Figure 3c). In those areas where higher amount of Fe was detected within the Si-rich matrix, distinct reflections in the SAED patterns were observed (see insets in Figures 3b–3d), evidencing the presence of crystalline materials. Analysis of the SAED patterns (*d*-spacings of approx. 0.145, 0.253 and 0.413 nm) together with the EDX mapping suggest the presence of an iron oxide/hydroxide phase(s) (e.g., goethite, magnetite). This is confirmed by HRTEM images showing

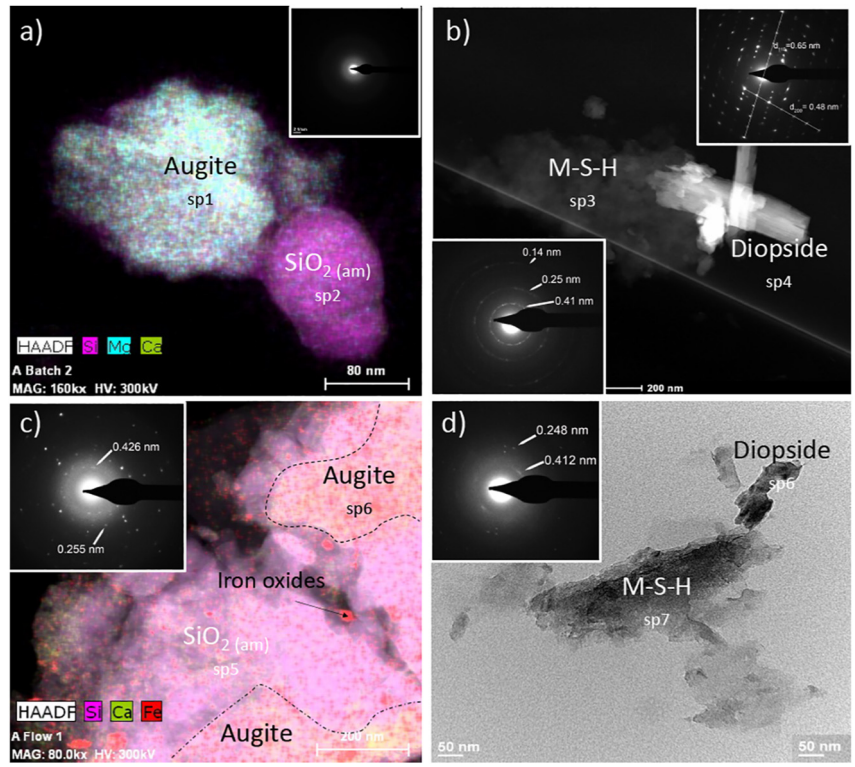

Figure 3. HRTEM analysis of reacted samples. (a) HAADF image overlaid with EDS elemental map of batch reacted augite product phases. The upper right inset shows the SAED pattern of the Si-rich zone. The diffuse halos confirm this phase is amorphous. (b) HAADF image of batch reacted diopside. SAED patterns of the different phases are shown in insets. (c) HAADF image overlaid with EDS elemental map of product phases after flow-through reaction highlighting the primary silicate, the amorphous SiO_2 phase and the iron oxides on the surface of the silica layer, responsible of the diffraction spots seen in the SAED pattern of the Si-rich zone (inset); (d) HRTEM image of partially reacted diopside after flow-through reaction. The inset shows the SAED pattern of the precipitated Si-rich phase. The spectra of each phase is shown in Figures S6–S9 in Supporting Information S1.

lattices fringes in nanoparticles embebed in an amorphous matrix, with an observed *d*-spacing that agrees with that of goethite ($d = 0.336$ nm, Figure S12 in Supporting Information S1, Shanker et al. (2011)). Alternatively, these *d*-spacings could correspond to poorly crystalline Mg-silicates similar to those reported by Zeyen et al. (2019).

Micro-CT analyses allow the direct visualization and quantification of the volume of amorphous silica formed in the weathering experiments (Figure 4 and Figure S13 in Supporting Information S1). Volume calculations showed that augite presents 9.6 vol. % SiO_2 (am) after batch weathering experiments, and 25.6 vol. % SiO_2 (am) after flow-through experiments. Diopside, on the contrary, showed much smaller silica contents in the reacted samples after both types of dissolution experiments (<1 vol % vs. 2.8 vol. %, for batch and flow-through runs, respectively). Micro-CT analysis showed a wide spatial distribution of amorphous silica all through the whole volume of reacted augite. Most of the pores and dissolution features of augite crystals were filled with amorphous silica, particularly in the case of flow-through experiments (Figure 4). Amorphous silica on the augite surface was only visible using this technique in the areas where cracks, which further propagated toward the interior of the crystal, initiated at or intersected with the mineral surface. Micro-CT analysis of diopside reacted in the flow-through system showed the same features observed in the case of augite. Pores and cracks were filled with amorphous silica, although a lower volume of this material was measured compared to augite runs. However, micro-CT observations of diopside crystals reacted in batch system showed no evidence of amorphous silica formation, possibly due to the limited resolution of this technique to detect nm-scale features (Figure 4).

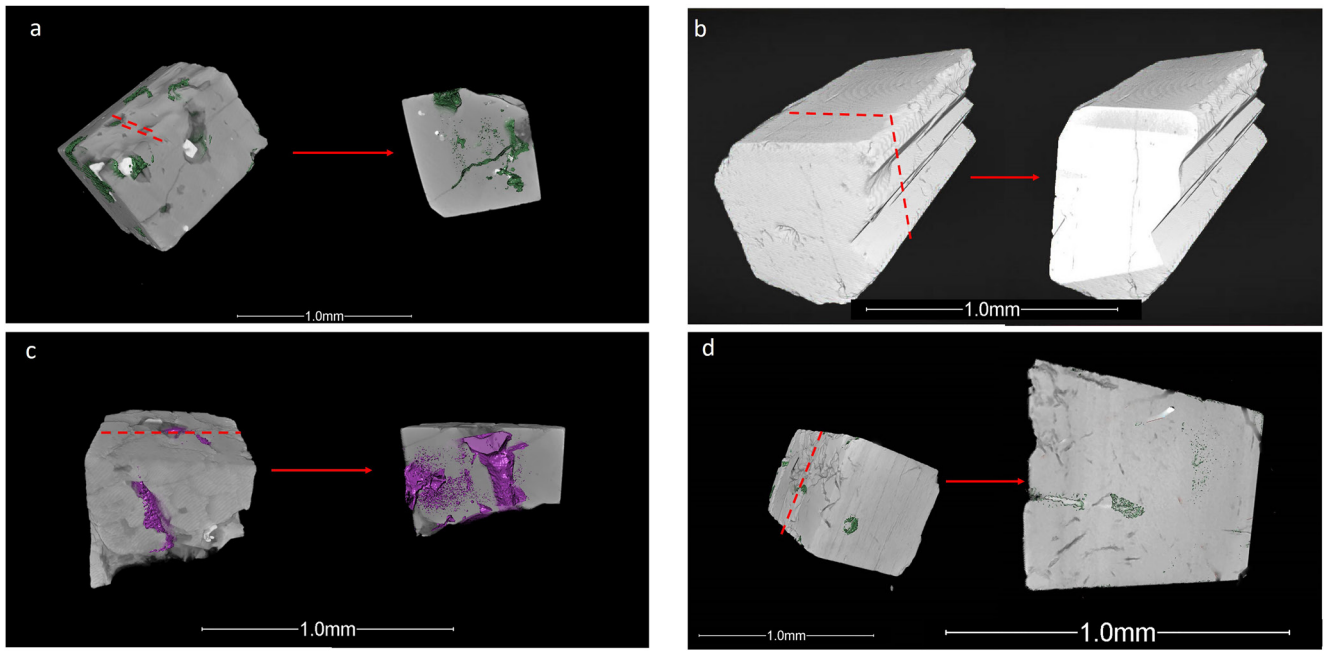

Figure 4. Micro-CT images of reacted pyroxene crystals with amorphous SiO_2 precipitate in color. Red dotted lines in the left images represent the virtual cut made to observe the interior of the reacted crystals, shown on the right. (a) Augite after batch experiments. (b) diopside after batch experiments. (c) augite after flow-through experiments. (d) diopside after flow-through experiments.

3.3. Kinetics of Element Release to the Solution

pH in flow-through experiments was constant (1.5) during the course of the experiments (10 h). In batch experiments, the pH increased up to 1.8 (diopside) and 2.1 (augite). Ca, Mg and Si fluxes during augite and diopside flow-through experiments showed the typical evolution as a function of time reported during silicate dissolution processes (e.g., Daval et al., 2010), with a steep decrease in the ion concentration in the first steps of the dissolution process, subsequently reaching a steady-state for both pyroxenes after ca. 200 min (Figure 5). Although stoichiometric steady state has been reported to be reached at much longer reaction times (e.g., diopside ~2,700 h at 25°C or ~100 h at 90°C for flow rates between 0.38 and 1.92 mL h^{-1}; Chen & Brantley, 1998), the significantly faster flow rate in our experiments (2 mL min^{-1}) speeds the rate of attainment of a steady state. Ca/Si and Mg/Si normalized elemental ratios in the outflow solutions were both different for augite and diopside (augite: 12.8–17.3 and 2.3–3.2, respectively; diopside: 9.0–12.3 and 1.8–2.4, respectively) (Figure 5 and Table S4 in Supporting Information S1). This apparent non-stoichiometric behavior can be explained by the formation of amorphous silica detected in our experimental analyses described above. At the same time, these elemental ratios were lower in batch dissolution experiments (augite: 2.9 and 1.0, respectively; diopside: 6.3 and 2.4, respectively) than in flow-through runs, which is consistent with the higher amount of SiO_2 (am) found in flow-through experiments. This nonstoichiometric behavior implies that dissolution rates calculated from Si release rates (r_{Si}), represent minimum values (Table S5 in Supporting Information S1). r_{Si} determined in batch experiments were lower than those measured in flow-through experiments (0.90 and 1.49 log units lower for augite and diopside, respectively) (Table S6 in Supporting Information S1). These differences arise from the fact that during the course of batch reactions, as the system approaches equilibrium, the driving force for dissolution decreases, and so do the dissolution rates. In batch experiments, the dissolution rate determined for augite was faster than for diopside (log r_{Si} (mol cm^{-2} s^{-1}) = -10.79 ± 0.04 and -11.20 ± 0.07 for augite and diopside, respectively). In flow-through experiments this trend was reversed: log r_{Si} (mol cm^{-2} s^{-1}) = -9.88 ± 0.02 and -9.71 ± 0.04 for augite and diopside, respectively (Tables S4–S6 in Supporting Information S1). This is related to the massive formation of amorphous silica in the case of augite weathered under continuous solution flow, which significantly decreases the Si flux measured during flow-through experiments. Under these conditions, the continuous supply of fresh solution over the mineral surface maintains the solution in contact with the mineral highly

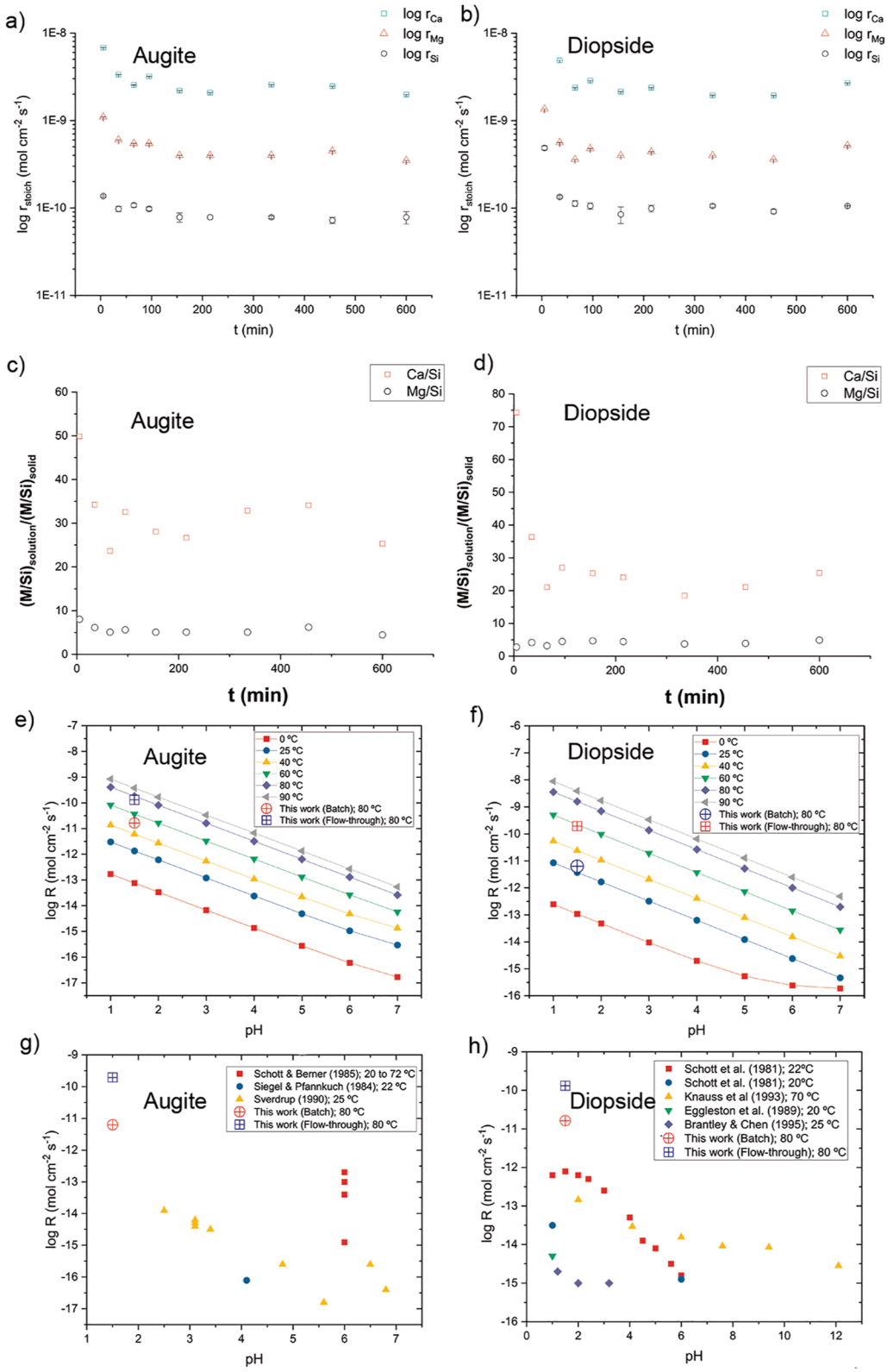
a)
Augite
log r_Ca
log r_Mg
log r_Si
log r_stoich (mol cm-2 s-1)
t (min)
b)
Diopside
c)
Ca/Si
Mg/Si
(M/Si)solution/(M/Si)solid
d)
e)
0 °C
25 °C
40 °C
60 °C
80 °C
90 °C
This work (Batch); 80 °C
This work (Flow-through); 80 °C
log R (mol cm-2 s-1)
pH
f)
g)
Schott & Berner (1985); 20 to 72 °C
Siegel & Pfannkuch (1984); 22 °C
Sverdrup (1990); 25 °C
h)
Schott et al. (1981); 22°C
Schott et al. (1981); 20°C
Knauss et al (1993); 70 °C
Eggleston et al. (1989); 20 °C
Brantley & Chen (1995); 25 °C

Figure 5.

undersaturated with respect to augite or diopside, allowing the fast release of silica units to the local fluid in contact with the mineral surface and the immediate buildup of supersaturation of the local fluid with respect to amorphous silica and its precipitation, which further removes Si from the fluid. This process can continue providing that fresh surface is exposed to the fluid, through the porous system of the precipitate layer or by the formation of cracks.

4. Discussion

During both flow-through and batch experiments, apparent incongruent dissolution was observed in all experiments (i.e., the elemental ratios measured in the solution differ from those measured in the solid, especially at the initial stages of dissolution; e.g., Daval et al., 2011). This apparent incongruent behavior arises from the formation of Si-rich phases (Casey et al., 1989; Hellmann et al., 2012). In this case, we observed a similar behavior not only at the outer mineral surfaces, but also further into the crystal, within cracks formed during dissolution. As explained above, most recent experimental studies suggest a mechanism of formation of these phases whereby they formed by tightly coupled interfacial dissolution–precipitation (e.g., Daval et al., 2009; Hellmann et al., 2012; Putnis, 2009; Ruiz-Agudo et al., 2016), initially controlled by the establishment of a steep compositional gradient at the mineral-fluid interface. Supersaturation with respect to amorphous silica can be reached in this interfacial fluid (Ruiz-Agudo et al., 2016). This ultimately depends on the relative rates of mass transport and surface reaction in the system, and strong compositional gradients are expected in those systems in which the kinetics of the surface reaction is fast relative to diffusion of dissolved species into the bulk solution.

Thermodynamic calculations performed using PHREEQC showed that bulk solutions in batch and flow-through experiments remain highly undersaturated with respect to both augite and diopside at the end of the experiments (Table S7 in Supporting Information S1). Additionally, batch and flow-through bulk solutions were undersaturated with respect to amorphous silica and M-S-H in all experiments performed, for both measured Si and the stoichiometric amount of Si (given by the measured concentrations of Ca and Mg). The saturation index with respect to amorphous silica and M-S-H varied from −0.89 to −2.17 and −27.43 to −36.12 for diopside and augite dissolution, respectively (Table S7 in Supporting Information S1). Therefore, bulk precipitation of amorphous silica or M-S-H is highly unlikely.

A comparison of the published far-from-equilibrium Si-based dissolution rates of the clinopyroxenes diopside and augite as a function of pH is shown in Figure 5. Also, values calculated using the dissolution rate law and rate parameters given by Palandri and Kharaka (2004), considering both acidic and neutral dissolution mechanisms, are plotted. The dissolution rates determined in this work were significantly higher than those determined experimentally in previous works, as most of them were collected at room T (Figure 5). However, despite the extensive formation of Si-rich secondary phases in augite during flow through experiments (25.6 vol% determined by Micro-CT), dissolution rates are in remarkably good agreement with those predicted for the relevant T (80°C) and pH from equations compiled in Palandri and Kharaka (2004). Flow-through determined rates for diopside differed though by 0.82 log units. As stated above, r_{Si} determined in batch experiments were lower than those measured in flow-through experiments, as in batch experiments the system is closer to equilibrium and therefore, the driving force for dissolution decreases. As shown in batch experiments, augite dissolves faster than diopside most likely due to its higher iron content. In chain silicates, reactivities are related to their chemical composition; typically, Ca-rich minerals are more reactive than Mg-rich phases (Marini, 2006), and previous works reported higher dissolution rates in iron-bearing pyroxenes as compared to non-iron-bearing pyroxenes (Hoch et al., 1996; Siever & Woodford, 1979). We suggest that the precipitation of Fe-oxides/hydroxides may remove iron from solution, thus promoting further dissolution of the Fe-bearing silicate. However, this behavior is masked by the more extensive

Figure 5. Dissolution rates for (a) augite and (b) diopside as a function of time in flow-through experiments using concentrations of Ca, Mg and Si measured in the outflow solutions, normalized to the stoichiometry of the initial solids. Elemental ratios as a function of time normalized to the ratios in the initial solids for (c) augite and (d) diopside flow-through experiments. Variation of (e) augite and (f) diopside dissolution rates (R) with pH, calculated using the dissolution rate law and rate parameters given by Palandri and Kharaka (2004), considering both acidic and neutral dissolution mechanisms. Values determined in this work are also plotted. Comparison of (g) augite and (h) diopside dissolution rates obtained in this work versus experimental published values (Brantley & Chen, 1995; Eggleston et al., 1989; Knauss et al., 1993; Schott & Berner, 1985; Schott et al., 1981; Siegel & Pfannkuch, 1984; Sverdrup, 1990).

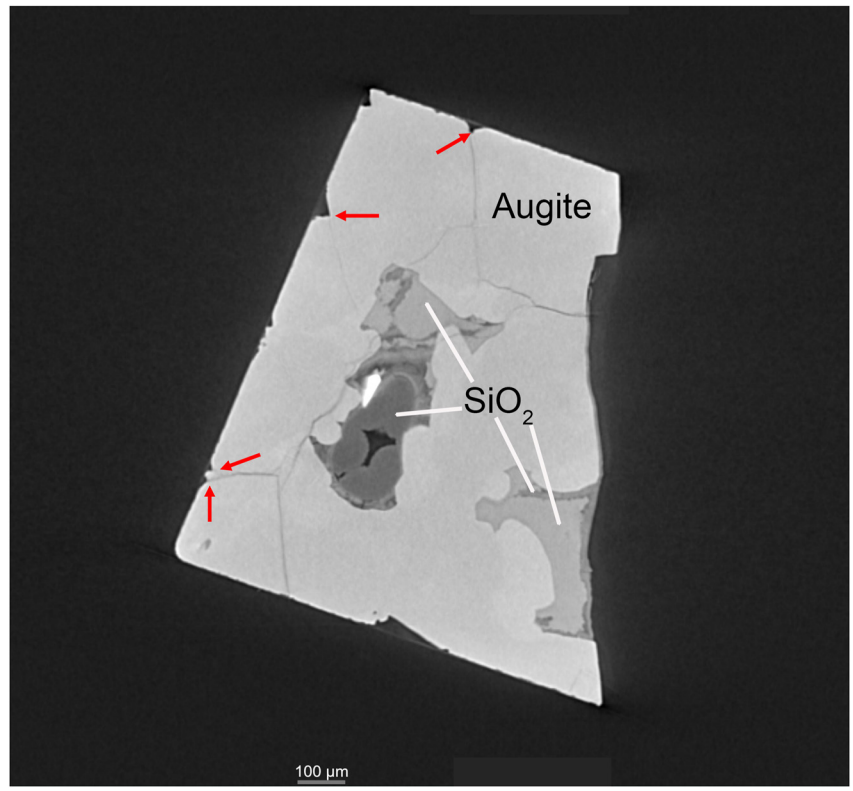

Figure 6. X-ray microtomography of a cross section of an augite crystal weathered in flow-through experiments at pH 1.5. Cracks initiated at high-curvature regions within dissolution pits are systematically observed (examples marked by the red arrows).

formation of Si-rich precipitates in the case of augite weathered under continuous solution flow. In this sense, Ca-based rates reflect better the actual kinetics of the congruent dissolution. In both batch and flow through experiments, Ca-based rates were higher for augite than diopside (see Tables S5 and S6 in Supporting Information S1).

The observed linear rate of silica release to solution with time has been reported as an indication of surface-limited dissolution in pyroxenes (Stumm, 1987). This behavior contrasts with our observations for wollastonite, in which the much faster dissolution rate of this pyroxenoid as compared to pyroxenes (~3 orders of magnitude) may result in the kinetics of the process being controlled by diffusion of dissolved species into the bulk solution (Ruiz-Agudo et al., 2016). In augite and diopside, compositional gradients between the mineral surface and the fluid would be flatter, and thus the precipitation of amorphous silica will be more limited. Although the formation of a homogeneous, thin surface layer all over the mineral surface (with thickness in or below the nm range) cannot be discounted, it is clear from our SEM and Micro-CT studies of the reacted samples that the thick and continuous Si-rich coatings found in wollastonite, do not form here. Interestingly, thick SiO_2 coatings seems to be limited to specific areas of the crystal surface and, more importantly, to the interior of cracks and other features most likely formed upon dissolution of the substrate. Singh and Gilkes (1993) reported similar observations on weathered samples of the pyroxene spodumene, which showed randomly oriented smectite in etch pits and cleavage cracks after the formation of an amorphous material, concluding that the dissolution of spodumene takes place through the complete breakdown of the structure involving a solution phase (i.e., stoichiometric dissolution) and the subsequent precipitation of an amorphous phase. In our samples, cracks initiated at surface features (etch pits and coalesced etch pits) formed upon stoichiometric dissolution (Figure 6) where stress will be concentrated within high-curvature regions (e.g. pit corners) (Plümper et al., 2012), and their propagation might be triggered by stress release. At etch pit corners and crack tips, strained Si-O bonds can react more readily with water compared to other areas with unstrained bonds (Atkinson, 1984). The presence of water in the liquid or

vapor states in these environments can trigger crack propagation by promoting weakening reactions. This mechanism is commonly known as stress corrosion (Atkinson, 1984), and is regarded as the preeminent mechanism explaining subcritical crack opening and propagation in rocks under shallow crustal conditions (Atkinson, 1984). Ultimately, this mechanism leads to intensive fracturing that generates fluid pathways to facilitate dissolution along the fracture surfaces, coupled with amorphous silica precipitation. The precipitation of an amorphous material is not expected to exert much stress due to the low critical supersaturation reached in the system and thus the resulting low crystallization pressure (Schiro et al., 2012). However, it has been suggested that the formation of an amorphous proto-serpentine phase during serpentinization of olivine could contribute to fracture propagation (Plümper et al., 2012). It could be argued that fracture propagation is facilitated in this case by a swelling mechanism similar to that leading to cement fracturing during the reaction of the alkaline solution in concrete pores with the siliceous minerals forming the aggregate (alkali-silica reaction, ASR, Rajabipour et al., 2015), rather than by the development of crystallization pressure. The theoretical maximum tensile strength for a crystal is ~E/10 (i.e., ~15–17 GPa for augite and diopside), although the actual value is typically much lower because of the presence of flaws (Idrissi et al., 2016). Indeed, stress values in the order of ca. 100 MPa are apparently enough for fracture opening in augite single crystals (Monasterio-Guillot et al., 2021). Experimental swelling pressures of up to 30 MPa have been reported for the hydration of amorphous silica gels (Reinhardt & Mielich, 2011). Our results show that even these low swelling pressures could result in fracture widening and propagation within augite and diopside crystals if stress corrosion occurs simultaneously.

Formation of SiO_2 at specific, limited areas of the mineral surface can be linked to highly defective areas or regions with a high step density, where the Si flux to the solution may be locally high. In a second scenario, i.e. within cracks and narrow dissolution features, ion diffusivities are expected to be significantly reduced with respect to the bulk solution. In both cases the build-up of high Si concentrations may be possible locally, which would allow supersaturation with respect to amorphous silica to be reached and its subsequent precipitation. The higher extent of secondary, Si-rich phase formation in weathered augite may be related to its faster dissolution as compared with diopside, linked to its higher iron content as discussed above. Additionally, a continuous fast flow of fresh solution over the mineral surface will maintain the solution in contact with the mineral highly undersaturated with respect to augite or diopside, so that the driving force for dissolution in flow-through dissolution experiments remains higher than in batch experiments during the course of these experiments. Far-from-equilibrium conditions, such as those in flow-through experiments, result in an increase in etch pit abundance which are the seed for crack nucleation and its subsequent propagation by stress corrosion and amorphous silica swelling (hydration) pressure. Fast enough flow rates ensure a high degree of undersaturation and allow the progress of the dissolution reaction and the formation of Si-rich phases within cracks of the crystal.

Interesting conclusions can be drawn from the results of the characterization of the secondary phases formed during the acidic dissolution of augite and diopside. First, the observation of the presence of Fe in the form of nanoparticles within the matrix of the amorphous silica phase provides direct evidence supporting an interface-coupled dissolution precipitation process as a mechanism for the formation of amorphous Si-rich phases during pyroxene weathering. By a solid-state, interdiffusional process is not possible to explain such a non-homogeneous distribution of iron in the SALs. Also, the Si-rich, Mg-bearing amorphous phase detected only in weathered diopside samples could possibly be an amorphous magnesium silicate hydrate (M-S-H) secondary phase. Note that the broad band observed in the 3,000–4,000 cm^{-1} region of the IR spectra of the diopside sample after batch experiments (Figure S14 in Supporting Information S1) can be associated with the asymmetrical stretching and bending vibrations of O-H bonds, respectively, indicating presence of Mg-OH and/or Fe-OH vibrations (Nye et al., 2021). Formation of M-S-H phases has been reported in numerous scenarios (Roosz et al., 2015 and refs therein), including some related to the alteration of silicate materials (e.g., cement and borosilicate glass) (Dauzeres et al., 2016; De Weerdt & Justnes, 2015; de Ruiter and Austrheim, 2017) and during the injection of CO_2-charged water into basalt (CarbFix project), where the predominant secondary mineral formed was a Mg-Fe-rich silicate phase (Oelkers et al., 2019). These phases show a wide compositional variation with Mg/Si ratios ranging from 0.2 up to 2 (Dauzeres et al., 2016; De Weerdt & Justnes, 2015), attributed to variations in the crystal structure of M-S-H phases. The ratios of the Si-rich, Mg-bearing phases formed in our experiments are in the lower limit of the values found in the literature, and within the range reported for borosilicate glass dissolution. Considering that

the formation of these phases is strongly favored at pH values above 8 (e.g., Hauksson et al., 1995), and since the bulk solution remain highly undersaturated with respect to M-S-H during all experiments, it can be hypothesized that such pH conditions are prevailing close to the mineral surface mostly during diopside dissolution, in agreement with the expected higher silica concentration in solution in this case compared to augite (since the amount of Si removed from solution by amorphous silica precipitation is lower). This could be an indirect indication of the high pH conditions prevailing at the diopside-solution interface, in contrast with those measured in the bulk. Note that even bulk pH values are higher for diopside than augite, although much more acidic than those required for M-S-H precipitation. Nevertheless, given the high difference in pH between bulk and interfacial fluids needed for M-S-H precipitation, this remains to be experimental proved by additional analysis, such as in situ phase shift interferometry or micro-pH electrode measurements. Finally, it should be considered that the formation of this M-S-H precursor, regardless of the exact mechanism by which it takes place, may reduce the yield of carbonation in diopside-bearing rocks used for CO_2 storage, due to the incorporation of Mg in the silica matrix, which is therefore not available for the precipitation of carbonates.

5. Conclusions and Implications

The results of this study show how under the far-from-equilibrium conditions prevailing in our experiments, pyroxene dissolution results in extensive etch pit formation, where cracks can initiate and propagate by stress corrosion and subsequent swelling of the precipitated silica gel. Fracture formation and propagation is essential to this weathering process, as it facilitates the transport of fluids within an otherwise impermeable material, exposes fresh pyroxene surfaces, and increases the fluxes of Ca and Mg released to the solution.

In contrast with other faster-dissolving silicate minerals, such as wollastonite, the formation of an amorphous Si-rich phase takes place mostly in highly localized areas of the mineral surface; mostly within deep etch pits and cracks. Although dissolution in pyroxenes is commonly surface-controlled, in these areas there is a low fluid renewal, and thus the reaction will be more likely controlled by transport of ionic species. This enables the local buildup of high Si-concentrations, and thus supersaturation with respect to amorphous silica can be reached locally. The faster reaction rate of augite compared to diopside, most likely due to its higher iron content, results in a greater amount of amorphous silica formation during augite dissolution, but also in a higher Ca and Mg release to the solution, feeding the system in alkaline-earth metals, susceptible to enhance the carbonate yield in the presence of a dissolved inorganic carbon (DIC) source.

Unlike augite, in the case of diopside the amorphous Si-rich phase incorporates significant amounts of Mg, so that the precipitate could be regarded as a M-S-H precursor. This is an indirect indication of the high pH conditions (>8) reached at the diopside surface during dissolution, quite different to those measured in the bulk. This is an experimental evidence demonstrating that the transformations that occurred in these systems could only be achieved by an ICDP mechanism, with the chemistry of the solution in contact with the reacting solid being very different from that of the bulk. Furthermore, it should be mentioned that targeting of augite-rich rocks would be favored as compared with diopside-bearing rocks for geological CO_2 storage, not only for its faster dissolution rates, but also because the incorporation of Mg into M-S-H formed after diopside will not be available for its precipitation as carbonates, acting as a handicap for an effective GCS strategy. Altogether, our results highlight relevant information to use in modeling GCS strategies to enhance the use of silicate-carbonation. Particularly, this study shed light on the relevance of the primary silicate mineral composition (Fe content) on the subsequent carbonate yield during CO_2 mineralization, as well as the importance of the hydrodynamics of the solution at controlling the progress of the silicate dissolution as the first step of CO_2 mineralization reaction. Our results are also relevant in other fields, and for example suggest that augite-bearing silicate building stones (e, g. basalts and gabbro or diorites) located in exposed areas of facades, where water flow is continuous, may be highly susceptible to weathering by acid rain.

Data Availability Statement

Data reported in this paper can be accessed at the Zenodo repository: https://doi.org/10.5281/zenodo.5498058.

Acknowledgments
This research has been funded by the Spanish Government (grant CGL2015-70642-R and CGL2015-73103-EXP), the European Commission (ERDF funds and ACT_ERA NET no. 691712, PCI2019-111931-2), the Junta de Andalucía (research group RNM-179), and the University of Granada (Unidad Científica de Excelencia UCE-PP2016-05). LMG acknowledges funding by the Spanish Government FPI (Grant BES-2016-078468). The authors also thank the personnel of the Centro de Instrumentación Científica (CIC; University of Granada) for assistance with ICP-OES, Micro-CT, and SEM analyses. All experimental results discussed here are presented in the main text and Supporting Information S1. The authors thank the anonymous reviewers for the extremely careful and fruitful revision performed, which has significantly improved the original version of the manuscript.

References

Atkinson, B. K. (1984). Subcritical crack growth in geological materials. *Journal of Geophysical Research*, *89*, 4077–4114. https://doi.org/10.1029/jb089ib06p04077

Banfield, J. F., Ferruzzi, G. G., Casey, W. H., & Westrich, H. R. (1995). HRTEM study comparing naturally and experimentally weathered pyroxenoids. *Geochimica et Cosmochimica Acta*, *59*, 19–31. https://doi.org/10.1016/0016-7037(94)00372-s

Berner, R. A., Sjoberg, E. L., Velbel, M. A., & Krom, M. D. (1980). Dissolution of pyroxenes and amphiboles during weathering. *Science*, *80207*, 1205–1206. https://doi.org/10.1126/science.207.4436.1205

Biswas, R., Khan, P., Mukherjee, S., Mukhopadhyay, A. K., Ghosh, J., & Muraleedharan, K. (2018). Study of short range structure of amorphous Silica from PDF using Ag radiation in laboratory XRD system, RAMAN and NEXAFS. *Journal of Non-Crystalline Solids*, *488*, 1–9. https://doi.org/10.1016/j.jnoncrysol.2018.02.037

Brantley, S. L., & Chen, Y. (1995). Chapter 4. Chemical weathering rates of pyroxenes and amphiboles. *Reviews in Mineralogy and Geochemistry*, *31*. 119–172. https://doi.org/10.1515/9781501509650-006

Casey, W. H., Westrich, H. R., Massis, T., Banfield, J. F., & Arnold, G. W. (1989). The surface of labradorite feldspar after acid hydrolysis. *Chemical Geology*, *78*, 205–218. https://doi.org/10.1016/0009-2541(89)90058-2

Chen, Y., & Brantley, S. L. (1998). Diopside and anthophyllite dissolution at 25deg and 90degC and acid pH. *Chemical Geology*, *147*, 233–248. https://doi.org/10.1016/s0009-2541(98)00016-3

Cliff, G., & Lorimer, G. (1975). The quantitative analysis of thin specimens. *Journal of Microscopy*, *103*(2), 203–207. https://doi.org/10.1111/j.1365-2818.1975.tb03895.x

Dauzeres, A., Achiedo, G., Nied, D., Bernard, E., Alahrache, S., & Lothenbach, B. (2016). Magnesium perturbation in low-pH concretes placed in clayey environment—Solid characterizations and modeling. *Cement and Concrete Research*, *79*, 137–150. https://doi.org/10.1016/j.cemconres.2015.09.002

Daval, D., Hellmann, R., Corvisier, J., Tisserand, D., Martinez, I., & Guyot, F. (2010). Dissolution kinetics of diopside as a function of solution saturation state: Macroscopic measurements and implications for modeling of geological storage of CO_2. *Geochimica et Cosmochimica Acta*, *74*, 2615–2633. https://doi.org/10.1016/j.gca.2010.02.003

Daval, D., Martinez, I., Guigner, J. M., Hellmann, R., Corvisier, J., Findling, N., et al. (2009). Mechanism of wollastonite carbonation deduced from micro- To nanometer length scale observations. *American Mineralogist*, *94*, 1707–1726. https://doi.org/10.2138/am.2009.3294

Daval, D., Sissmann, O., Menguy, N., Saldi, G. D., Guyot, F., Martinez, I., et al. (2011). Inuence of amorphous silica layer formation on the dissolution rate of olivine at 90degC and elevated pCO_2. *Chemical Geology*, *284*, 193–209. https://doi.org/10.1016/j.chemgeo.2011.02.021

de Ruiter, L., & Austrheim, H. (2017). Formation of magnesium silicate hydrate cement in nature. *Journal of the Geological Society*, *175*, 308–320. https://doi.org/10.1144/jgs2017-089

De Weerdt, K., & Justnes, H. (2015). The eect of sea water on the phase assemblage of hydrated cement paste. *Cement and Concrete Composites*, *55*, 215–222. https://doi.org/10.1016/j.cemconcomp.2014.09.006

Dixit, S., & Carroll, S. A. (2007). Eect of solution saturation state and temperature on diopside dissolution. *Geochemical Transactions*, *8*, 1–14. https://doi.org/10.1186/1467-4866-8-3

Dove, P. M., Han, N., Wallace, A. F., & De Yoreo, J. J. (2008). Kinetics of amorphous silica dissolution and the paradox of the silica polymorphs. *Proceedings of the National Academy of Sciences*, *105*, 9903–9908. https://doi.org/10.1073/pnas.0803798105

Eggleston, C. M., Hochella, M. F., Jr, & Parks, G. A. (1989). Sample preparation and aging effects on the dissolution rate and surface composition of diopside. *Geochimica et Cosmochimica Acta*, *53*, 797–804. https://doi.org/10.1016/0016-7037(89)90026-4

Frings, P. J., & Buss, H. L. (2019). The Central Role of Weathering in the Geosciences. *Elements: An International Magazine of Mineralogy, Geochemistry, and Petrology*, *15*, 229–234. https://doi.org/10.2138/gselements.15.4.229

Fu, X., Wang, A., & Krawczynski, M. J. (2017). Characterizing amorphous silicates in extraterrestrial materials: Polymerization effects on Raman and mid-IR spectral features of alkali and alkali earth silicate glasses. *JGR Planets*, *122*, 839–855. https://doi.org/10.1002/2016je005241

Hamilton, V. E. (2000). Thermal infrared emission spectroscopy of the pyroxene mineral series. *Journal of Geophysical Research*, *105*, 9701–9716. https://doi.org/10.1029/1999je001112

Hauksson, T., Pórhallsson, S., Gunnlaugsson, E., & Albertsson, A. (1995). Control of magnesium silicate scaling in district heating systems. In *Proceedings World Geothermal Congress*. Florence (pp. 2487–2490).

Hellmann, R., Wirth, R., Daval, D., Barnes, J. P., Penisson, J. M., Tisserand, D., et al. (2012). Unifying natural and laboratory chemical weathering with interfacial dissolution-reprecipitation: A study based on the nanometer-scale chemistry of uid-silicate interfaces. *Chemical Geology*, *294–295*, 203–216. https://doi.org/10.1016/j.chemgeo.2011.12.002

Hoch, A. R., Reddy, M. M., & Drever, J. I. (1996). The eect of iron content and dissolved O_2 on dissolution rates of clinopyroxene at pH 5.8 and 25 C: Preliminary results. *Chemical Geology*, *132*, 151–156. https://doi.org/10.1016/s0009-2541(96)00050-2

Idrissi, H., Bollinger, C., Boioli, F., Schryvers, D., & Cordier, P. (2016). Low-temperature plasticity of olivine revisited with in situ TEM nanomechanical testing. *Science Advances*, *2*, e1501671. https://doi.org/10.1126/sciadv.1501671

Karlsson, C., Zanghellini, E., Swenson, J., Roling, B., Bowron, D. T., & Borjesson, L. (2005). Structure of mixed alkali/alkaline-earth silicate glasses from neutron diraction and vibrational spectroscopy. *Physical Review B: Condensed Matter*, *72*, 64206. https://doi.org/10.1103/physrevb.72.064206

Knauss, K. G., Nguyen, S. N., & Weed, H. C. (1993). Diopside dissolution kinetics as a function of pH, CO_2, temperature, and time. *Geochimica et Cosmochimica Acta*, *57*, 285–294. https://doi.org/10.1016/0016-7037(93)90431-u

Marini, L. (2006). *Geological sequestration of carbon dioxide: Thermodynamics, kinetics, and reaction path modeling*. Elsevier.

Meyer, N. A. (2014). *An investigation into the dissolution of pyroxene: A precursor to mineral carbonation of PGM tailings in South Africa*. Thesis.

Monasterio-Guillot, L., Di Lorenzo, F., Ruiz-Agudo, E., & Rodriguez-Navarro, C. (2019). Reaction of pseudowollastonite with carbonate-bearing uids: Implications for CO_2 mineral sequestration. *Chemical Geology*, *524*, 158–173. https://doi.org/10.1016/j.chemgeo.2019.06.011

Monasterio Guillot, L., Fernández Martínez, A., Ruiz Agudo, E., & Rodriguez Navarro, C. (2021). Carbonation of calcium-magnesium pyroxenes: Physical-chemical controls and effects of reaction-driven fracturing. *Geochimica et Cosmochimica Acta*, *304*, 258–280. https://doi.org/10.1016/j.gca.2021.02.016

Nye, S. A., Vineet, S., Oze Christopher, O., Barnaby, S., & Chris, C. (2021). Use of olivine for the production Of MgO-SiO_2 Binders. *Frontiers in Built Environment*, *7*, 640243. https://doi.org/10.3389/fbuil.2021.640243

Oelkers, E. H., Butcher, R., Pogge von Strandmann, P. A. E., Schuessler, J. A., von Blanckenburg, F., Snaebjornsdottir, S. O., et al. (2019). Using stable Mg isotope signatures to assess the fate of magnesium during the in situ mineralisation of CO_2 and H_2S at the CarbFix site in SW-Iceland. *Geochimica et Cosmochimica Acta*, *245*, 542–555. https://doi.org/10.1016/j.gca.2018.11.011

Omori, K. (1971). Analysis of the infrared absortion spectrum of diopside. *American Mineralogist*, *56*, 1607–1616.

Palandri, J. L., & Kharaka, Y. K. (2004). *A compilation of rate parameters of water-mineral interaction kinetics for application to geochemical modeling*. Geological Survey Menlo Park CA.

Parkhurst, D. L., & Appelo, C. A. J. (1999). User's guide to PHREEQC (Version 2): A computer program for speciation, batch-reaction, one-dimensional transport, and inverse geochemical calculations. *Water Resources Investigations Report*, *99*(4259), 312.

Plümper, O., Royne, A., Magraso, A., & Jamtveit, B. (2012). The interface-scale mechanism of reaction-induced fracturing during serpentinization. *Geology*, *40*, 1103–1106.

Putnis, A. (2009). Mineral replacement reactions. *Reviews in Mineralogy & Geochemistry*, *70*, 87–124. https://doi.org/10.2138/rmg.2009.70.3

Rajabipour, F., Giannini, E., Dunant, C., Ideker, J. H., & Thomas, M. D. A. (2015). Alkali–silica reaction: Current understanding of the reaction mechanisms and the knowledge gaps. *Cement and Concrete Research*, *76*, 130–146. https://doi.org/10.1016/j.cemconres.2015.05.024

Reinhardt, H. W., & Mielich, O. (2011). A fracture mechanics approach to the crack formation in alkali-sensitive grains. *Cement and Concrete Research*, *41*, 255–262. https://doi.org/10.1016/j.cemconres.2010.11.008

Richet, P., Mysen, B., Ingrin, J., Pascal, R., & Mysen, B. O. (1998). High temperature X-ray diraction and Raman spectroscopy of diopside and pseudowollastonite. *Physics and Chemistry of Minerals*, *25*, 401–414. https://doi.org/10.1007/s002690050130

Roosz, C., Grangeon, S., Blanc, P., Montouillout, V., Lothenbach, B., Henocq, P., et al. (2015). Crystal structure of magnesium silicate hydrates (MSH): The relation with 2: 1 Mg–Si phyllosilicates. *Cement and Concrete Research*, *73*, 228–237. https://doi.org/10.1016/j.cemconres.2015.03.014

Ruiz-Agudo, E., King, H. E., Patino-Lopez, L. D., Putnis, C. V., Geisler, T., RodriguezNavarro, C., & Putnis, A. (2016). Control of silicate weathering by interface-coupled dissolution precipitation processes at the mineral-solution interface. *Geologica*, *44*, 1–4. https://doi.org/10.1130/g37856.1

Ruiz-Agudo, E., Putnis, C. V., & Putnis, A. (2014). Coupled dissolution and precipitation at mineral-uid interfaces. *Chemical Geology*, *383*, 132–146. https://doi.org/10.1016/j.chemgeo.2014.06.007

Schiro, M., Ruiz-Agudo, E., & Rodriguez-Navarro, C. (2012). Damage mechanisms of porous materials due to in-pore salt crystallization. *Physical Review Letters*, *109*, 265503. https://doi.org/10.1103/physrevlett.109.265503

Schott, J., & Berner, R. A. (1985). Dissolution mechanisms of pyroxenes and olivines during weathering. In *The chemistry of weathering* (pp. 35–53). Springer. https://doi.org/10.1007/978-94-009-5333-8_3

Schott, J., Berner, R. A., & Sjoberg, E. L. (1981). Mechanism of pyroxene and amphibole weathering – I. Experimental studies of iron-free minerals. *Geochimica et Cosmochimica Acta*, *45*, 2123–2135. https://doi.org/10.1016/0016-7037(81)90065-x

Schott, J., Pokrovsky, O. S., Spalla, O., Devreux, F., Gloter, A., & Mielczarski, J. A. (2012). Formation, growth and transformation of leached layers during silicate minerals dissolution: The example of wollastonite. *Geochimica et Cosmochimica Acta*, *98*, 259–281. https://doi.org/10.1016/j.gca.2012.09.030

Shanker, U., Bhushan, B., Bhattacharjee, G., & Kamaluddin (2011). Formation of nucleobases from formamide in the presence of iron oxides: Implication in chemical evolution and origin of life. *Astrobiology*, *11*, 225–233. https://doi.org/10.1089/ast.2010.0530

Shao, H., Thompson, C. J., Qafoku, O., & Cantrell, K. J. (2013). In Situ Spectrophotometric Determination of pH under Geologic CO_2 Sequestration Conditions: Method Development and Application. *Environ. Sci. Technol. 47*, 63–70.

Siegel, D. I., & Pfannkuch, H. O. (1984). Silicate mineral dissolution at pH 4 and near standard temperature and pressure. *Geochimica et Cosmochimica Acta*, *4840*, 197–201. https://doi.org/10.1016/0016-7037(84)90362-4

Siever, R., & Woodford, N. (1979). Dissolution kinetics and the weathering of mac minerals. *Geochimica et Cosmochimica Acta*, *43*, 717–724. https://doi.org/10.1016/0016-7037(79)90255-2

Simão, J., Ruiz-Agudo, E., & Rodriguez-Navarro, C. (2006). Effects of particulate matter from gasoline and diesel vehicle exhaust emissions on silicate stones sulfation. *Atmospheric Environment*, *40*, 6905–6917.

Singh, B., & Gilkes, R. J. (1993). Weathering of spodumene to smectite in a lateritic environment. *Clays and Clay Minerals*, *41*, 624–630. https://doi.org/10.1346/ccmn.1993.0410513

Stockmann, G., Wolff-Boenisch, D., Gislason, S. R., & Oelkers, E. H. (2008). Dissolution of diopside and basaltic glass: The eect of carbonate coating. *Mineralogical Magazine*, *72*, 135–139. https://doi.org/10.1180/minmag.2008.072.1.135

Stumm, W. (1987). *Aquatic surface chemistry: Chemical processes at the particle-water interface*. John Wiley & Sons.

Sverdrup, H. U. (1990). *The kinetics of Base cation release due to chemical weathering*. Lund Univ Press.

Weissbart, E. J., & Rimstidt, J. D. (2000). Wollastonite: Incongruent dissolution and leached layer formation. *Geochimica et Cosmochimica Acta*, *64*, 4007–4016. https://doi.org/10.1016/s0016-7037(00)00475-0

Wojdyr, M. (2010). Fityk: A general-purpose peak tting program. *Journal of Applied Crystallography*, *43*, 1126–1128. https://doi.org/10.1107/s0021889810030499

Yang, X., Roonasi, P., & Holmgren, A. (2008). A study of sodium silicate in aqueous solution and sorbed by synthetic magnetite using in situ ATR-FTIR spectroscopy. *Journal of Colloid and Interface Science*, *328*, 41–47. https://doi.org/10.1016/j.jcis.2008.08.061

Zeyen, N., Benzerara, K., Menguy, N., Brest, J., Templeton, A. S., Webb, S. M., et al. (2019). Fe-bearing phases in modern lacustrine microbialites from Mexico. *Geochimica et Cosmochimica Acta*, *253*, 201–230. https://doi.org/10.1016/j.gca.2019.03.021